Decomposition of AVIRIS Spectra: Extraction of Surface-Reflectance, Atmospheric, and Instrumental Components

Lisa R. Gaddis, Laurence A. Soderblom, Hugh H. Kieffer, Kris J. Becker, James Torson, and Kevin Mullins

***Abstract*— We present techniques that use only information contained *within* a raw, high-spectral-resolution, hyperspectral Airborne Visible/Infrared Imaging Spectrometer (AVIRIS) scene to estimate and remove additive components (atmospheric scattering and instrument dark current). These techniques allow normalization of multiplicative components (instrument gain, topography, atmospheric transmission) and enhancement, extraction, and identification of relative-reflectance information related to surface composition and mineralogy. Our derivation of additive components from raw AVIRIS data is based on an adaptation of Crippen's "regression intersection method (RIM)." As does RIM, we use pairs of surface units that are spectrally homogeneous, spatially extensive, and located in rugged terrain. However, our technique utilizes the long-wavelength spectral data of AVIRIS to derive and remove atmospheric scattering components *for each unit*. AVIRIS data from the Kelso Dunes and Granite Mountain areas of southern California served as spectrally contrasting, topographically modulated surfaces for illustration of this technique. For a given site and wavelength pair, subtraction of the wavelength-dependent additive component from individual bands will remove topographic shading in both sites in band-to-band ratio images. Normalization of all spectra in the scene to the average scene spectrum results in cancellation of multiplicative components and produces a relative-reflectance scene. Absorption features due to mineral absorptions that depart from the average spectrum can be identified in the relative-reflectance AVIRIS product. The validity of these techniques is demonstrated by comparisons between relative-reflectance AVIRIS spectra derived from application of this technique and those derived by using the standard calibration techniques of JPL. Calibrated spectra were extracted from an AVIRIS scene of the Upheaval Dome area of Canyonlands National Park, UT. Results show that surface-reflectance information can be extracted and interpreted in terms of surface mineralogy after application of these techniques to AVIRIS data.**

I. Introduction

A MAJOR purpose of imaging spectrometers operating in visible and near-infrared wavelengths is to measure the spectral reflectance of the Earth's surface to study its composition. Such measured radiance has interacted along its path length with both the atmosphere and the target surface, and thus it is affected by instrumental, atmospheric, and ground characteristics in additive and multiplicative combinations. Extraction of surface reflectance information from imaging spectrometer data requires removal or compensation for the additive and multiplicative components [1]–[5]. Major spectral components that contribute additively include atmospheric scattering (e.g., measured radiance scattered within the atmosphere only, both before and after surface reflection) and the instrument dark current; multiplicative components include solar flux, two-way atmospheric transmission, topographic effects, and instrument gain. Instrument gain and atmospheric scattering are also included in the multiple-scattering additive components.

Many techniques used to derive surface reflectance from imaging spectrometer data rely on external information, such as assumptions about instrument behavior or measurements of atmospheric and ground surface characteristics [1], [5]–[7]. A perspective gained from planetary science (a field in which ground-truth information is difficult or impossible to obtain) emphasizes the need for data-dependent analytical techniques for estimation and treatment of the various components in a remotely acquired spectrum, both for obtaining surface mineralogical information and for providing an independent check on instrument calibration. In this analysis, the objective is to use only information contained *within* a single, high-spectral-resolution, hyperspectral scene to quantify and remove additive components, to deal with multiplicative components through normalization of all spectra in the scene to the average scene spectrum (resulting in production of a relative-reflectance scene), and to extract information on the mineralogy and composition of surface geologic units. Our paper presents the basic elements of these techniques as applied to Airborne Visible/Infrared Imaging Spectrometer (AVIRIS) data (~0.4 to 2.4 μm) acquired over an area with relatively simple geology, the Kelso Dunes area of the eastern Mojave Desert, CA. Support for the validity of these techniques is presented through comparisons of AVIRIS relative-reflectance spectra derived from application of this technique and data radiometrically calibrated using the standard techniques of the Jet Propulsion Laboratory (JPL; i.e., raw DN to radiance) [8], [9]. Radiometrically calibrated data were normalized by a nominal solar spectrum and presented in units of scaled irradiance/solar flux (I/F) for more direct comparison to surface and sample spectra. Calibrated spectra were extracted from an AVIRIS scene of the geologically complex Upheaval Dome

Manuscript received May 12, 1994; revised November 9, 1994. This work was supported by NASA/Goddard Grants S-19867-E (EOS/HIRIS) and S-46459-E (EOS/ASTER). ISIS software development was supported by JPL Contract WO-8654.

The authors are with U.S. Geological Survey, Flagstaff, AZ 86001 USA.

Publisher Item Identifier S 0196-2892(96)00289-6.

0196–2892/96$05.00 © 1996 IEEE

area of Canyonlands National Park, UT. Upheaval Dome has a controversial origin as either an impact crater remnant [15] or a salt dome [16]; it provides an interesting illustration of the utility of our technique for remote investigations of surface mineralogy.

In the simplest form, additive-component correction techniques can fail because they assume implicitly that atmospheric scattering is the same from area to area within a hyperspectral scene (e.g., [3]). The approach described here extends previous work in that it demonstrates and utilizes the natural, elevation-dependent variation in atmospheric column height to derive separate solutions for atmospheric scattering for different regions. To validate these techniques, the solutions are decomposed into Rayleigh, Mie, and instrument dark-current components. Use of these techniques not only allows decoupling of atmospheric scattering from surface reflectance, it also provides an independent check on the instrument behavior through analyses of the instrument dark-current. These methods can be applied to many of the terrestrial and planetary imaging spectrometer data sets (e.g., OMEGA on Mars 96, VIMS on Cassini, SSI and NIMS on Galileo, EOS/ASTER on Earth) for analyses of surface reflectance, atmospheric scattering, and instrument behavior.

II. AVIRIS Data Characteristics

The data used in this analysis were acquired over the Kelso Dunes area (34°55′ N, 115°43′ W) of the Mojave Desert, CA, in 1987 and the Upheaval Dome area (38°27′ N, 109°55′ W) of Canyonlands National Park, UT, in 1991 by the NASA/JPL AVIRIS instrument. AVIRIS consists of an opto-mechanical scanner with four spectrometers (A–D) that view the surface simultaneously with ~10-nm bandpasses in 224 contiguous spectral channels from 0.4 to 2.45 μm [8]. The precision (described as the instrument reference radiance divided by its signal-to-noise requirement, or the "noise-equivalent delta radiance," NEΔL) of these AVIRIS data is as follows: ~0.2 for the A detector, ~0.08 for the B detector, and ~0.05 for the C and D detectors for the 1987 data; ~0.1 for the A detector and ~0.05 for the B, C, and D detectors for the 1991 data. An AVIRIS "scene" is 614 pixels wide, 512 lines long, and 224 bands deep. The spectral sampling interval for each band is nominally 10 nm. With an Instantaneous-Field-of-View (IFOV) of 1.12 mrad, and at typical aircraft speeds (e.g., 730 km/h) and altitudes (e.g., 20 km), the spatial sampling of the AVIRIS data are 17 m × 17 m at nadir and the spatial response function is 20 m along-track and 21 m across-track, resulting in ~20 m × 20 m image spatial resolution [10], [11].

A raw AVIRIS spectrum (measured in digital numbers or DN's) includes the ground-reflection spectrum that contains surface compositional information, but this information is obscured heavily by instrumental and atmospheric spectral components. Before distribution from JPL, raw AVIRIS data are subjected commonly to a series of processing steps designed to suppress or remove effects of spectrometer misalignments, overlapping bands, geometric distortions, the influence of longer path-lengths in the outer parts of the sensor optics ("vignetting"), the additive effects of the instrument dark current (the base-level or "dark" response of the instrument), and laboratory instrument response [10], [11]. Such radiometrically calibrated AVIRIS data are distributed in units of scaled radiance (μWcm^{-2} nm^{-1}sr^{-1}).

In this paper we start with raw AVIRIS data, estimate and remove the additive components, compensate for the multiplicative components, and compare our "internally calibrated" results with spectra extracted from AVIRIS data that have been radiometrically calibrated by the standard JPL techniques. Prior to compositional analysis, dropped lines and unusable bands (including low-signal bands, bands in the strong water-vapor absorptions centered at 0.94, 1.14, 1.38, and 1.88 μm, and redundant bands where detectors overlap), are identified and set to null values.

III. Fundamental Concepts

In simple terms, six major, wavelength-dependent components of a typical spectrum acquired in visible and near-infrared wavelengths must be dealt with to derive surface reflectance from measured raw data (Fig. 1) [12]. The components are the following: solar flux (F); atmospheric transmission (T); surface reflectance (R); atmospheric scattering ($A\uparrow$ and $A\downarrow$, irradiance at the top and bottom of the atmosphere, respectively); the instrument gain (G); and the instrument dark current (D). The solar flux is a relatively well known quantity due to our knowledge of both the time-dependent behavior of solar irradiance and the time-of-day of data acquisition. The atmospheric transmission has characteristic "windows" through which spectral observations can be made, but they vary in "clarity" with atmospheric aerosol content, mostly water vapor [13]. The surface reflectance (as related to mineral composition) is the quantity we seek; it is influenced by a variety of parameters, including slope and roughness of the terrain and particle size, texture, composition, and moisture content of surface materials. Atmospheric scattering varies with the amounts and types of particulates and gas molecules in the atmosphere; its influence decreases with increasing wavelength. Instrument gain and dark-current parameters characterize the sensor response; in this analysis the gain is assumed to be linear, and both the dark current and the gain are assumed to be constant within the image. These components (Fig. 2) combine in additive and multiplicative ways to form a measured spectrum.

The largest portion of energy in a measured raw spectrum is the direct-reflected component (Fig. 2), which incorporates multiplicatively the solar flux, two-way atmospheric transmission, surface reflectance, surface photometric function (P), and instrument gain. In rugged terrain, the surface reflectance incorporates the effects of topography, because it modulates incident and reflected solar radiation. The photometric properties of the surface define the lighting geometry and thus the light-scattering behavior of the surface [14]; they are a function of viewing phase (α), incidence (i), and emission (ε) angles. The direct-reflected component, written $FT^2RP\ (\alpha, i, \varepsilon)G$, contains the surface-reflectance information that we seek.

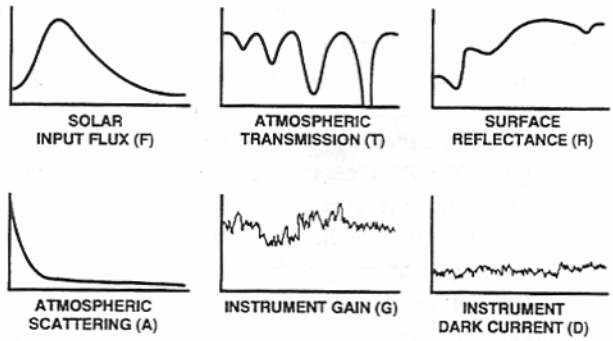

Fig. 1. Common spectral components of the visible and near-infrared wavelengths shown at the same relative-reflectance scale.

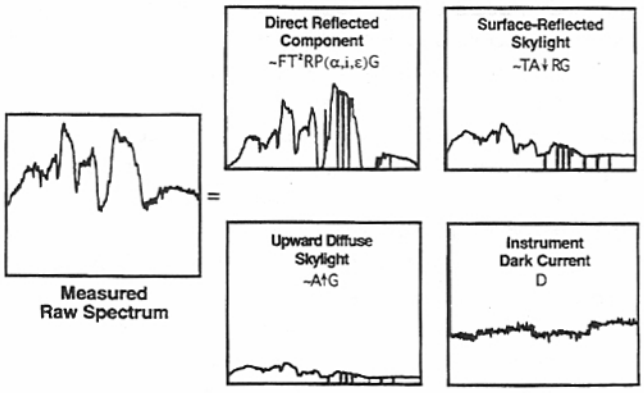

Fig. 2. Major combined spectral components of the visible and near-infrared wavelengths shown at the same relative-reflectance scale.

A second major component is surface-reflected skylight (Fig. 2), the diffuse light scattered to the surface through multiple interactions with the atmosphere and surface that is reflected directly back to the sensor. Surface-reflected skylight includes upward atmospheric transmission, downward-scattered radiation at the bottom of the atmosphere (A↓, which incorporates the solar flux and downward atmospheric transmission), surface reflectance, and instrument gain, and it can be written $TA{\downarrow}RG$. The other major additive component in a measured raw spectrum is upward diffuse skylight ($A{\uparrow}G$, where $A{\uparrow}$ incorporates the solar flux and two-way atmospheric transmission), also called path radiance or haze. This diffuse skylight is mostly due to atmospheric scattering, although the surface is weakly involved where it contributes to the multiple scattering at the base of the atmosphere. In general, both surface-reflected skylight and upwelling diffuse skylight contribute most significantly to the measured spectrum at short wavelengths. In practice, these two terms are not separable, and together they compose the atmospheric scattering component. The last major additive component of a spectrum is the instrument dark current (D), a measure of instrument background noise that elevates the spectrum by a set of wavelength-dependent constant values (Fig. 3). These four relations can be expressed as

$$\text{Raw spectrum} = (FT^2RPG) + [(TA{\downarrow}RG) + (A{\uparrow}G)] + D \quad (1)$$

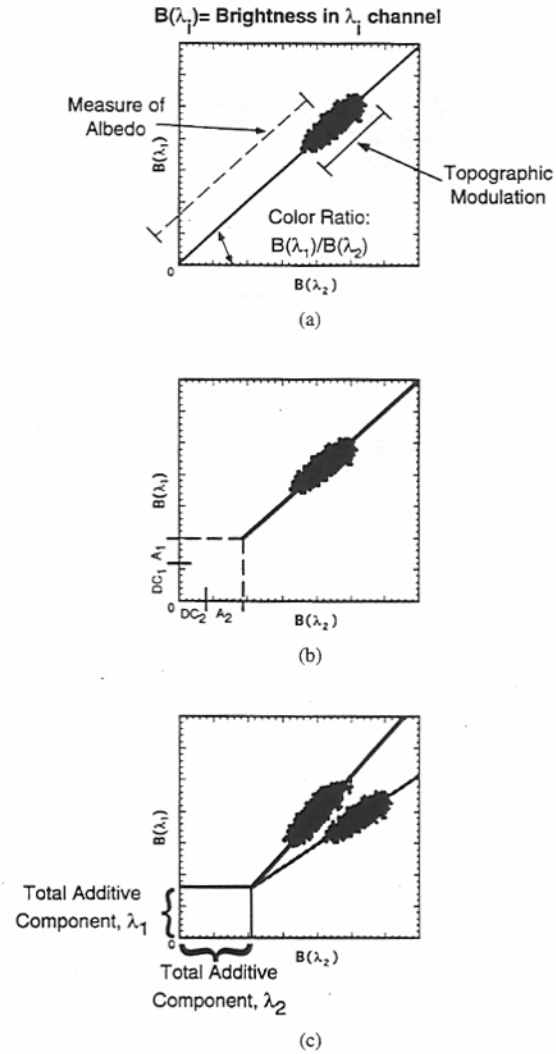

Fig. 3. The 2-D histogram method of solution for additive components. (a) Pixel brightness values from "ideal" or calibrated data with no atmospheric or instrument effects. Plot shows a 2-D histogram of pixels from a spectrally homogeneous, topographically modulated unit at two wavelengths. A line fit through the histogram passes through the plot origin representing zero illumination and zero reflectance. (b) For data with additive components [such as atmospheric scattering (A) and the instrument dark current (DC)], the intersection point moves away from the origin by an amount equal to the additive component values at each wavelength. (c) Without additional information about the additive components at a given wavelength, two subareas that have different intrinsic albedoes must be used to determine the total additive components for each wavelength.

where the first is the multiplicative term we seek and the last three are additive terms.

The atmospheric scattering components can be approximated further by

$$A{\downarrow} \approx c_1 FTr \quad (2)$$

and

$$A{\uparrow} \approx c_2 FT^2 r \quad (3)$$

where r is the effective reflectance of the multiple-scattering (atmosphere-surface) environment and c_1 and c_2 are coefficients related to differences in the overall scattering levels

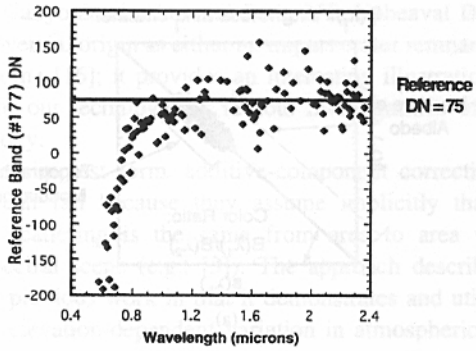

Fig. 4. Calculated intercept values for reference band 177 (wavelength = 1.98 μm) versus all other bands for Granite Mountains and Kelso Dunes sites. Note that the intersection values decrease and are not stable at wavelengths shorter than $\sim$1.4 μm. A stable intersection value (DN$\sim$75) is established only at longer wavelengths.

due to asymmetry in the scattering functions and to attenuation. These approximations are appropriate for an optically thin atmosphere, but they neglect the complex reality of the integral interactions of absorption and scattering at the surface-atmosphere interface. Nevertheless, these approximations provide a useful illustration of the composition of the spectral components. Substitution of (2) and (3) in (1) allows the total radiance to be represented by

$$\text{Raw spectrum} \approx FT^2G(RP + c_1Rr + c_2r) + D \qquad (4)$$

which illustrates that if the instrument dark current is well known, the raw spectrum can be normalized to a reference spectrum from the scene (e.g., an average of some area) to yield a quantity that relates only to the reflectance properties of the surface (R) and atmosphere (r). We will use this form subsequently in extracting the total approximate atmospheric additive signal from the raw AVIRIS spectra.

The procedure to extract relative surface-reflectance information from raw AVIRIS data requires only information contained *within* a single scene and forces the data to be internally consistent. The first step in the process is to derive and remove the total additive components $[(TA{\downarrow}RG) + (A{\uparrow}G) + D]$ and then to compensate for multiplicative components $(FT^2RP(\alpha, i, \varepsilon)G)$ by using normalization and ratioing techniques to derive relative reflectance (i.e., relative to a reference spectrum in the scene).

IV. Additive Components

Our technique for derivation of additive-component spectra from a raw AVIRIS scene is an extension of the "regression intersection method (RIM)" of Crippen [3]. The RIM uses selected pairs of units in a multispectral image that are spectrally homogeneous (each with a contrasting, dominant reflectance or albedo), spatially extensive (e.g., $>10^2$ pixels), and located in rugged terrain (i.e., they have a strong brightness modulation due to topography). Starting with two spectral bands substantially separated in wavelength, two-dimensional histograms of pixel DN values for two areas are produced. Regression lines are fitted to these histograms for each area; their intersection point represents the sum of all additive terms for those wavelengths. Intersection values are derived for several band pairs across a scene and for all bands. Median values of intersection points are then subtracted to remove scene-average values of additive components at all wavelengths. The RIM additive components are limited in their accuracy by this averaging process and because they are derived with the implicit assumption that atmospheric components (i.e., scattering and transmission) are the same for all areas of the scene. We note that this is an invalid assumption.

Our recognition of this fundamental limitation led us to investigate the application of an adaptation of the RIM to the high-spectral-resolution, multiwavelength AVIRIS data. As outlined in detail below, a fundamental aspect of our adaptation is the recognition that a stable intersection-point value exists at longer wavelengths where atmospheric components are less significant. This stable value, which is very similar to the instrument dark-current for a given band, is used as a reference value to calculate intersection values for shorter wavelengths and thus to derive total additive components and atmospheric scattering spectra *which are different for each site*. After removal of the known dark-current spectrum, *we derive additive component spectra separately for each site*, something that was not possible using the simpler RIM technique. We have been able to deconvolve the raw AVIRIS spectra into dark-current, atmospheric scattering, and direct-reflected components, to remove these total additive components while accounting for differences in atmospheric components within a scene, and thereby to derive more accurate surface reflectance spectra.

To clarify the extent of our adaptation of the RIM, we present a brief summary of Crippen's method, followed by a relatively simple application of our technique to two units in a single AVIRIS scene from the Mojave Desert, CA (parts of the Granite Mountains and Kelso Dunes). Before presenting the results, some basic characteristics of such two-dimensional histograms will be discussed. First, consider the case of spectral data for a surface with no atmosphere and zero dark-current values (e.g., orbital data of the Moon). If pixels are plotted from a spectrally homogeneous, topographically modulated unit from such a surface at two different wavelengths, they would form an elongated, two-dimensional histogram cluster. The absolute albedo of the unit is related directly to the distance of the cluster center from the origin; the elongation of the cluster represents the variation in pixel brightness introduced by topography, and the slope of the line through the cluster is controlled by the color ratio between the two wavelength bands (Fig. 5(a)). For the case of data for a surface with no atmosphere and zero dark-current levels, a line fit through such a two-dimensional histogram passes through the plot origin representing zero illumination and zero reflectance. For data with additive components, this intersection point moves away from the origin (Fig. 5(b)), and two subareas that have different intrinsic albedoes must be used to determine the additive components for each wavelength (Fig. 5(c)). These additive terms must be subtracted before spectral reflectance

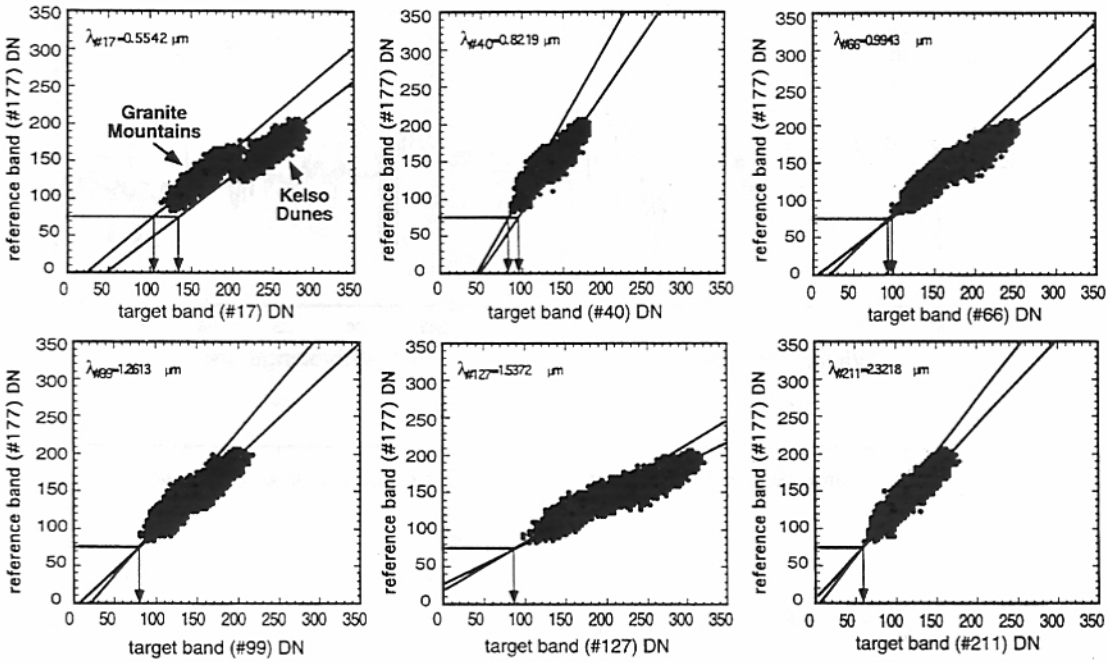

Fig. 5. 2-D histograms of pixel brightness values for the Granite Mountains and Kelso Dunes sites. For a reference DN value of 75 for the two sites, intercept values at shorter wavelengths are higher and divergent, and at longer wavelengths they are lower and convergent. At shorter wavelengths, the high intercept values are indicative of the different amounts of additive components (primarily due to elevation differences) for each site. At longer wavelengths (beyond the additive-component effects), the intercepts converge to stable values that are comparable with the instrument dark-current values.

is linearly related to illumination intensity. To correct for the effects of total additive components in an entire spectral scene, it is generally assumed that the atmosphere over the scene is homogeneous (again, we know this to be invalid) and that variation in surface reflectance as it affects the surface-reflected skylight can be neglected. If a scene contains many units that are widespread, contrasting in brightness, spectrally homogeneous, and topographically modulated, a total additive spectrum may be derived that is a more accurate representation of either the scene-average total additive spectrum or its local variability.

If the RIM criteria for the calibration sites are not met, the relations discussed above will not hold. Specifically, if the chosen units are not spectrally homogeneous, then the two-dimensional histograms will form irregular clusters (i.e., mixed spectral classes) and may overlap excessively, and regression lines will not be valid. If topographic modulation is not present or is insufficient, the histograms will not be elongated, and calculated regression lines will either be invalid or have significant errors. If insufficient spectral contrast is observed among units, the histograms will overlap and the points of intersection will be unstable (i.e., small differences in regression-line slopes between overlapping histograms can result in large fluctuations in the intercept values). In these cases, additional information is needed to identify a valid reference DN value. This analysis excludes all band pairs with regression lines and/or 2-D histograms that have intersections at angles of $\leq 10°$ and $>75°$ and that have inadequate topographic modulation (i.e., insufficient spread about a histogram centroid). The linear regression method used here calculates a line through a two-dimensional histogram by principal-components rotation, minimizing the rms residual measured perpendicularly to the line of fit (i.e., the principal-component axis with the largest eigenvalue) [17].

To illustrate the failure of RIM for our AVIRIS Mojave Desert scene, we selected a single reference band and we calculated and plotted corresponding intersections for every other band (Fig. 4). The reference band should be a long-wavelength (to minimize atmospheric effects), clean (low-noise) band that is not located in or near a water band; band 177 (wavelength = 1.9848 μm) has been used for this example. As outlined above in the case of a surface with no atmospheric variance within the scene, we would expect the intersection offset for the reference band from all band-pair solutions to be approximately constant. In fact, a plot of intersection points for the Kelso Dunes and Granite Mountains units with reference band 177 paired with all other bands shows that the intersection-point solution decreases and is not stable at wavelengths shorter than about 1.4 μm. A reasonably constant reference-band intersection value (in this case, ~75 DN) is established only at longer wavelengths (Fig. 4). The scatter in these values is expected and is due to noisy bands (e.g., near water bands and spectral regions of low atmospheric transmission), minor spectral heterogeneities in the selected sites, and instrument response (gain and dark current) variations. This behavior indicates that a stable intersection-point solution exists at longer wavelengths for a single (i.e., reference) band paired with all other bands; this reference value is comparable with the dark-current value (DN = 77) for this band. Recognition of stability in the intersection

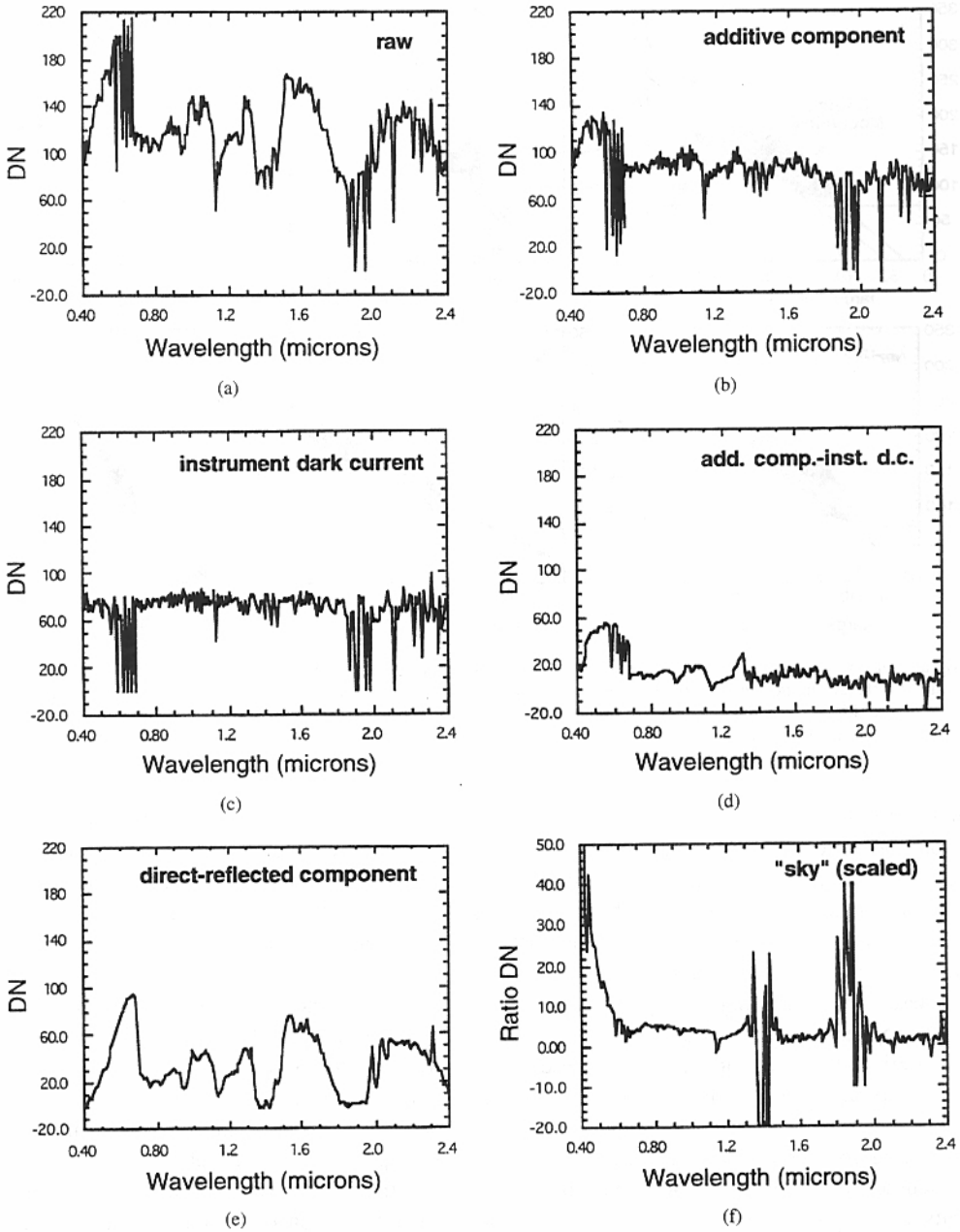

Fig. 6. Decomposition of Granite Mountains AVIRIS spectra: (a) raw spectrum; (b) derived additive component; (c) instrument dark current; (d) additive component minus the instrument dark current; (e) the direct-reflected component (raw minus the additive component); and (f) the derived "sky" component (the ratio of the additive and the direct-reflected components; note the reduced scale). At a higher elevation (~6738′) with less atmospheric thickness, the Granite Mountains site has less atmospheric scattering (particularly at shorter wavelengths) than the Kelso Dunes site (elevation ~2600′; see Fig. 10). Noisy regions of the spectra are primarily caused by atmospheric water absorptions (e.g., at 1.8 μm).

point solutions at longer wavelengths removes the necessity of calculating intersection values for all possible site-pair and band-pair combinations. Furthermore, as outlined below, use of the known dark-current spectrum allows us to deconvolve the additive-component spectrum for a particular site into atmospheric scattering and dark-current values, and thus to characterize the behavior of the atmospheric column in a given area.

Our use of a reference value for characterizing the additive component at shorter wavelengths revealed distinct differences in the intersection-point solutions for the two different sites. For example, using the reference value of DN = 75, the two-dimensional histograms for the Granite Mountains and Kelso Dunes units show, at shorter wavelengths, intersection points that have higher DN values and are more widely divergent; at longer wavelengths these intersections have lower DN values and converge to similar values (Fig. 5). For each site, a plot of these intersection DN values (all bands versus reference band) with respect to wavelength represents an additive-component spectrum (Figs. 6(b) and 7(b)). The additive-component spec-

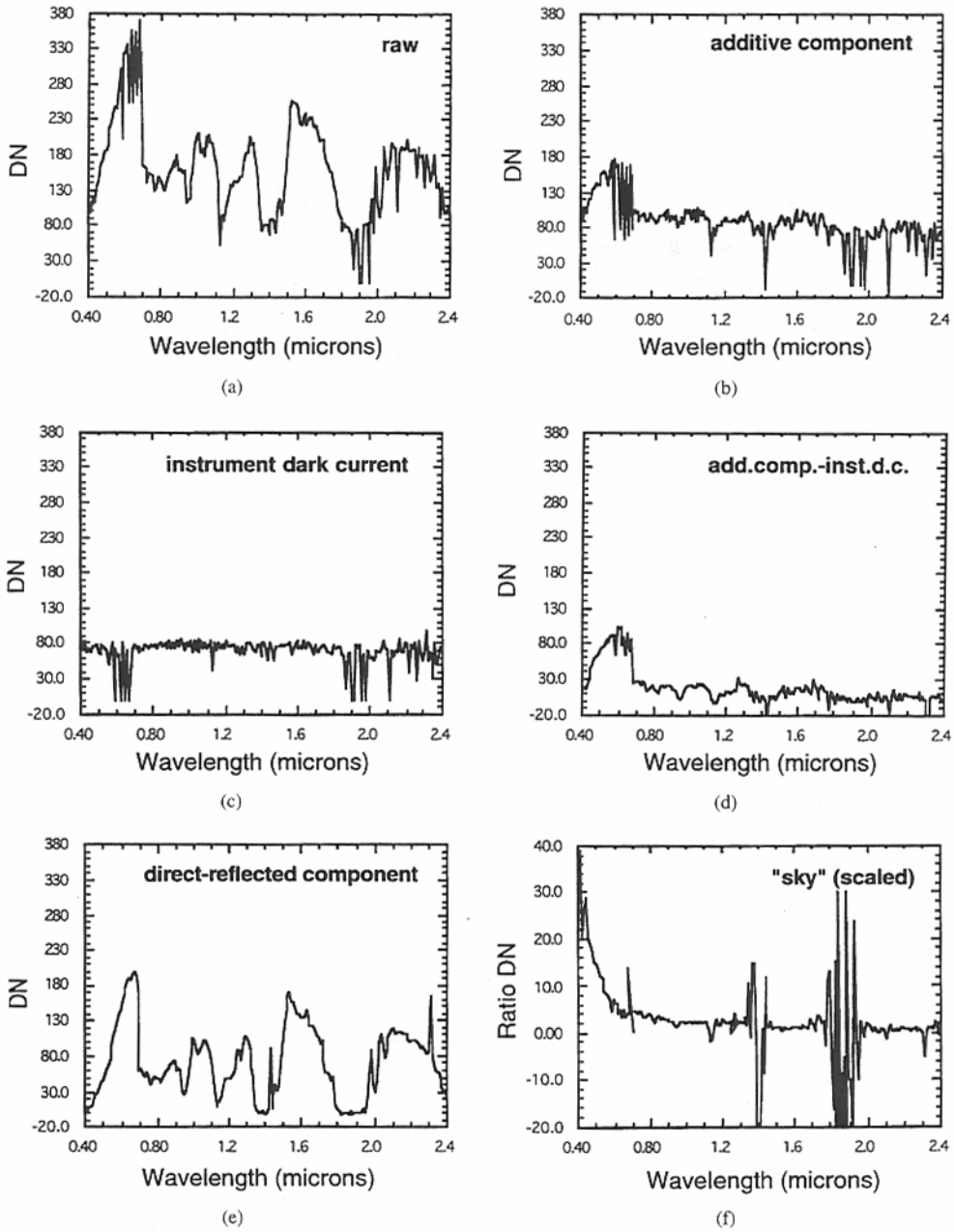

Fig. 7. Decomposition of Kelso Dunes AVIRIS spectra: (a) raw spectrum; (b) derived additive component; (c) instrument dark current; (d) additive component minus the instrument dark current; (e) the direct-reflected component (raw minus the additive component); and (f) the derived "sky" component (the ratio of the additive and the direct-reflected components; note the reduced scale).

tra for the Granite Mountains and Kelso Dunes units show strongly similar values at longer wavelengths and distinctly different values at shorter wavelengths. These differences at smaller wavelengths are attributable to the differences in atmospheric column height between the two sites due to their differences in elevation; the Granite Mountains site (elevation = ~6738′) shows less atmospheric scattering than the Kelso Dunes site (elevation = ~2600′). As expected, the calculated total additive component spectra (Figs. 6(b) and 7(b)) for each of the two units in the Mojave AVIRIS scene resemble a combined noisy atmospheric-scattering spectrum and an instrument dark-current spectrum.

The character of the total additive spectrum can be understood through examination of atmospheric scattering behavior and the measured AVIRIS instrument dark current (Figs. 6–8). Rayleigh theory describes scattering for particles with diameters that are small with respect to the incident wavelength (e.g., gas molecules). For Rayleigh scattering, the amount of scattering is inversely proportional to λ^{-4}, so that more radiation is scattered at short wavelengths [13]. For larger particles (e.g., aerosols, smoke, dust), Mie theory is applicable and scattering is less selective with respect to λ, approaching a λ^{-1} dependence. At long wavelengths in an AVIRIS spectrum, atmospheric scattering of solar radiation

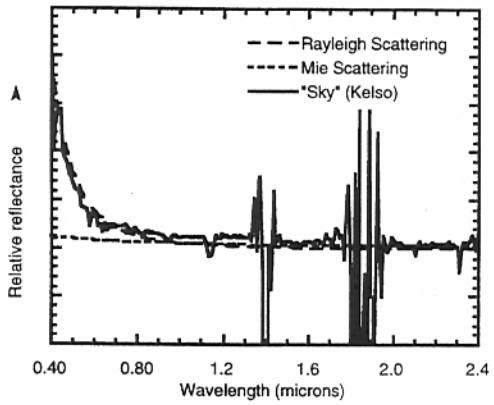

Fig. 8. Comparison of the derived "sky" component (the ratio of the additive and the direct-reflected components) for the Kelso Dunes area and the Rayleigh and Mie atmospheric scattering models. Note that the "sky" spectrum resembles both the standard Rayleigh ($\lambda \leq 1$ μm) and Mie ($\lambda > 1$ μm) scattering components. Noisy regions of the Kelso spectrum are primarily caused by atmospheric water absorptions (e.g., at 1.8 μm).

is expected to follow Mie theory. For calculated additive component spectra at shorter wavelengths, intercept values are expected to be higher at shorter wavelengths due to Rayleigh scattering. To illustrate this in more detail, we can extract an approximate spectrum from the additive component that is due dominantly to atmospheric scattering alone (a "sky" color spectrum). First, we assume that the surface observed is flat ($P \sim 1$) and that it has a bland or "gray" reflectance (R is a constant, typically $\sim$0.2). Second, we estimate the direct-reflected spectral component (FT^2RPG, or FT^2G) by subtracting the calculated additive component ($TA{\downarrow}G + A{\uparrow}G + D$) from a raw spectrum [$FT^2G = \text{Raw} - (TA{\downarrow}G + A{\uparrow}G + D)$]. Next, subtraction of the instument dark-current spectrum (provided independently) from the calculated total additive component spectrum gives an atmospheric scattering spectrum [$TA{\downarrow}G + A{\uparrow}G$, or $FT^2Gr(c_1 + c_2)$]. Finally, we divide the atmospheric scattering spectrum by the direct-reflected component (FT^2G), and the multiplicative terms (FT^2G) cancel, yielding an approximate atmospheric scattering only or "sky" spectrum [$A{\downarrow}{\sim}r(c_1 + c_2) \propto r$], where r is the effective reflectance of the multiple scattering (atmosphere-surface) environment (see (4)). Note that the "sky" spectrum has elements resembling both the combined standard Rayleigh ($\lambda \leq 1$ μm) and Mie ($\lambda > 1$ μm) scattering components (Fig. 8).

V. Multiplicative Components

A. Method

Subtracting the calculated total additive-component spectrum from raw AVIRIS data removes the additive effects of atmospheric scattering and the instrument dark current, and the total direct-reflected component remains. In addition to the surface-reflectance information that we seek, the direct-reflected component (FT^2RPG) still contains the multiplicative influences of topography (including the effects of terrain roughness and the geometry of instrument viewing and solar illumination), atmospheric transmission, and instrument gain. These influences can be removed through two normalization procedures to arrive at relative reflectance (cf. "internal average relative" reflectance of Kruse [18]). Derivation of relative reflectance from a raw AVIRIS scene from Upheaval Dome is presented here. The Upheaval Dome area was chosen for this analysis because it has excellent exposures of geologic units; the sedimentary units (sandstones, shales, limestones, conglomerates) are expected to have identifiable spectral absorption features in the AVIRIS wavelength range (0.4 to 2.4 μm); and it is the focus of intensive field and laboratory spectral analyses intended to aid in understanding AVIRIS hyperspectral data [19]. The origin of Upheaval Dome is controversial: salt doming [16], [20], cryptovolcanic [21], and impact [14], [22] origins have all been proposed for this structure. The origin of Upheaval Dome will not be addressed in this study.

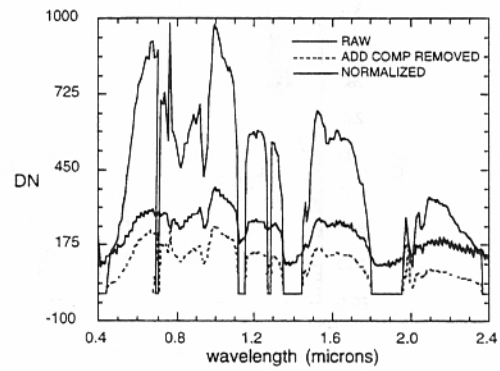

(a)

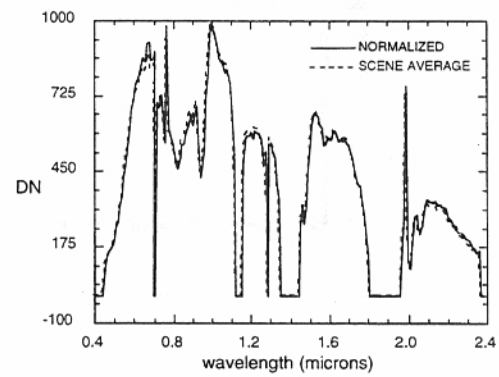

(b)

Fig. 9. Processed AVIRIS spectra of the Upheaval Dome area, UT. (a) Comparison of raw, additive-component removed, and normalized spectra. (b) Comparison of normalized versus scene-average spectra.

Most of the differences in pixel brightness among units in a direct-reflected component spectral image are due to differences in unit albedo and in illumination due to topography. These variations in brightness mask the intrinsic unit reflectances, and they must be suppressed to make the relative-reflectance information apparent. We used an equal-area normalization to scale the sum of all of the DN's in each spectrum to a constant, arbitrary value [18]. Such an

operation effectively scales the variation in broadband albedo among the units in a scene to a common value of overall brightness, and it thereby mutes the influence of topography on the relative brightnesses of the units (Fig. 9(a)). The resulting image data should be examined to determine the effectiveness of this procedure in removing image topography.

At this point, the normalized data still retain the effects of atmospheric transmission and instrument gain. The procedure to remove these remaining multiplicative terms is to normalize the data again, this time by dividing each spectrum by an average scene spectrum [18]; the FT^2G term will cancel out, resulting in the reflectance of the surface relative to a scene average value (Fig. 9(b)). As pointed out by Kruse [18] and Clark and King [23], it is important to remember that the average scene spectrum may have features related to mineral absorptions as well as features due to atmospheric transmission and instrument gain. The average scene spectrum should be examined for the presence of possible mineral absorptions by comparing it with the product FT^2G estimated from atmospheric models and bench calibration data.

The resulting relative-reflectance spectra have two major components that are related to surface composition and that must be interpreted separately. Broad-band, low-frequency components (e.g., the "continuum" of Clark and Roush [24]) are believed to be the complex products of factors such as wavelength-dependent scattering [25] or a single dominant surface component that produces a significant spectral slope (e.g., the "red slope" of lunar soil spectra [26]). A continuum may simply represent absorptions due to different minerals or to different absorption processes in the mineral of interest. In practice, a continuum function is removed commonly from spectra of terrestrial and planetary surfaces to enhance the expression of specific, often weak mineral absorption features [19], [24], [26], [27].

Of greater interest to geologists are the smaller, shorter frequency features produced by specific mineral absorptions. To identify possible mineral absorption features in the relative-reflectance spectra in this analysis, we used a $3 \times 3 \times 3$-pixel (sample$\times$line$\times$band), low-pass filter to suppress small-scale (high-frequency) "noise" and then a $1 \times 1 \times 15$-pixel, high-pass filter to enhance the strength of the relatively weak absorption features by removing long-wavelength variations (Fig. 10). After features are visually identified with the enhanced filtered data, however, unfiltered data are then compared with laboratory spectra (by using a spectrum-matching technique) and can be used to derive images that are interpretable in terms of relative-absorption band strengths and positions, and thus surface mineralogy.

B. Application: Upheaval Dome

Upheaval Dome (diameter ~5 km), located on the Colorado Plateau in Utah, consists of complexly faulted sedimentary rocks that form a central dome surrounded by a structurally depressed ring (Fig. 11) [14], [28]. Doming has inverted the stratigraphic order of the exposed formations, and they are listed here in this order (from the exterior to the interior): the Kayenta Formation (Lower Jurassic), Wingate Sandstone (Lower Jurassic), Chinle Formation (Upper Triassic), Moenkopi Formation (Middle and Lower Triassic), White Rim Sandstone (Lower Permian), and Organ Rock Formation (Lower Permian) (modified from [29]; Table I). Clastic dikes of crushed sandstone from the White Rim Sandstone are intruded near the center of the dome [28].

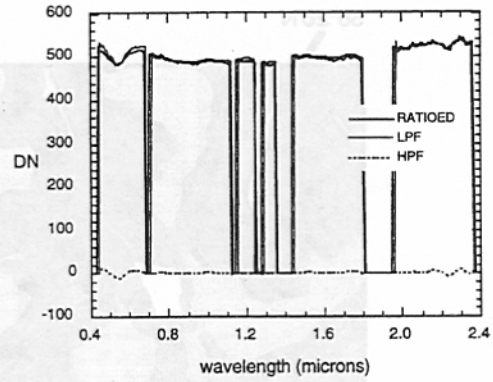

Fig. 10. Processed AVIRIS spectra of the Upheaval Dome area, UT: Comparison of ratios ("relative reflectance"), low-pass filtered (LPF), and high-pass filtered (HPF) spectra.

The procedures described above for derivation of relative-reflectance information were applied to the Upheaval Dome AVIRIS data. Certain aspects of the character of these data, however, required modifications in the application of the techniques. More specifically, inadequate spectral contrast is observed among units at long wavelengths for the Upheaval Dome AVIRIS scene, causing intercept values to be unstable. At shorter wavelengths, the spectral contrast in these data is greater, so a reference band at long wavelengths and a test band at shorter wavelengths were used to calculate intercept values for derivation of additive-component spectra.

As an alternative to this reference band-versus-test band intercept value, we also examined the known dark current and a representative spectrum of a shadowed area. If one assumes that the "shade" spectrum contains only atmospheric effects, with no contribution from surface reflectance [4], then the difference between the dark-current and shade values should represent the atmospheric additive component at that wavelength, including the amount of atmospheric scattering and/or absorption. For example, the dark-current value at band 29 (0.6774 μm) in the AVIRIS data is 91 DN, and the "shade" value is ~133 DN. The atmospheric additive component for band 29 is thus ~42 DN. Two areas in the Upheaval Dome AVIRIS image were identified that yielded intercept values at band 29 and a long-wavelength reference band (177, 1.9848 μm) that were as close as possible to the known shade values at those wavelengths. For bands 29 and 177, shade values are 133 DN and 121 DN and calculated intercepts are 135 and 124, respectively. Through such comparisons with the shade values, the intercepts for the two test sites were interpreted to represent valid reference values that could be used to derive additive-component spectra.

In support of this technique for estimating the atmospheric scattering component from shade values, the calculated

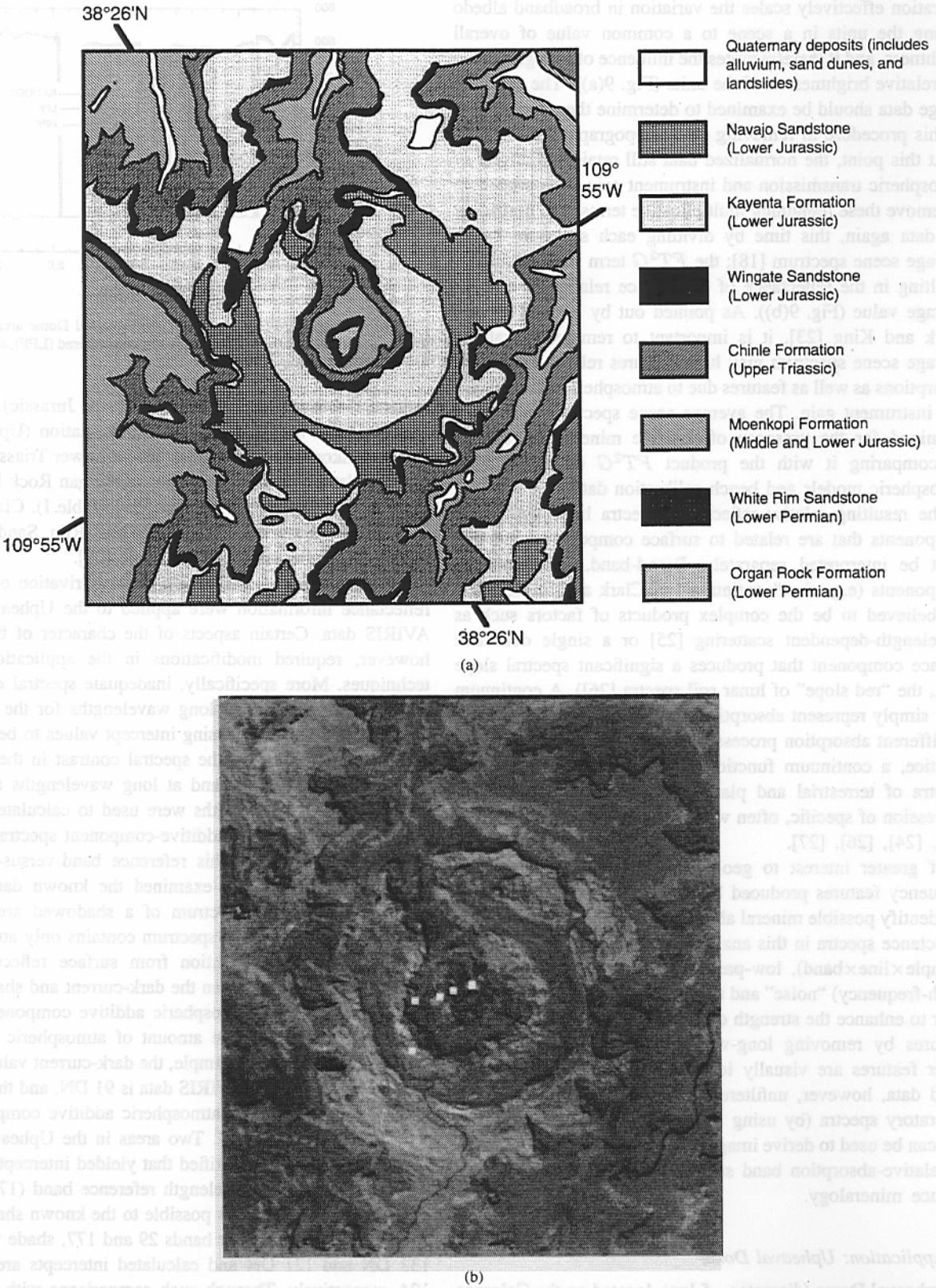

Fig. 11. Upheaval Dome, UT. (a) Geologic sketch map (after Huntoon *et al.*, 1982; see Table I for geologic descriptions). (b) AVIRIS image (sites from which spectra were extracted are marked; band 75, wavelength = 1.08 μm; flight $\doteq$ 20, run = 1, segment = 2; ~18 : 57, 5/20/91; scale is 1 cm = 0.4 km).

additive-component spectra closely resemble the "shade" spectrum [4]. The additive-component spectrum that most closely matched the "shade" spectrum (component 2) was then subtracted from the AVIRIS data to remove the dark

TABLE I
LITHOLOGY AND DETECTABLE MINERALOGY OF MAJOR GEOLOGIC FORMATIONS OF THE UPHEAVAL DOME AREA, UT

Formation	Lithology**	Mineralogy	Thres-hold	Band Depth	Goodness of Fit
Kayenta	sandstone interbedded with subordinate siltstone, limestone, and shale (reddish brown)	hematite	0.05	0.070	0.954
Chinle	bentonitic clayey sandstone and siltstone, local conglom-eratic sandstone (red, purple, green)	hematite	0.05	0.088	0.987
Moenkopi	ripple-marked, cross-laminated siltstone and sandstone (reddish brown)	muscovite kaolinite	0.10 0.10	0.102 0.099	0.940 0.912
White Rim	fine-grained, cross-bedded sandstone (light gray)	kaolinite	0.15	0.040	0.913
Organ Rock	siltstone and sandy shale (reddish brown)	kaolinite muscovite	0.15 0.15	0.043 0.051	0.967 0.868

* Order of formations is from exterior to interior of dome. The Wingate Sandstone, a cliff-forming unit stratigraphically intermediate between the Kayenta and Chinle Formations, is not prominent in the AVIRIS data and was excluded from this analysis.

** After Huntoon et al., 1982.

current and as much as possible of the atmospheric scattering effects (Fig. 12). In partial validation of this procedure, a residual image formed by ratioing bands 29 and 177 with valid additive components removed showed little or no remaining topographic effects (the residual image was formed by subtracting 135 DN and 124 DN from bands 29 and 177, respectively).

Representative spectra from each of five major geologic formations of Upheaval Dome were extracted from the raw, relative-reflectance (low-pass filtered), and calibrated (scaled intensity/solar flux, I/F) AVIRIS data (Fig. 13). (The Wingate Sandstone was excluded from this analysis because its outcrop is relatively small.) Because of the presence of diagnostic absorption features from major sedimentary rock-forming minerals and their weathering products [30]–[32] and the lack of water absorptions, we will focus on interpretation of these extracted spectra in the wavelength ranges of 0.45–0.65 μm and 2.0–2.3 μm. In all cases, the raw spectra are dominated by atmospheric scattering, and few mineral absorptions are observed. The relative-reflectance spectra, however, show a variety of absorption bands in these wavelength ranges of 0.45–0.65 μm and 2.0–2.3 μm. Relative to a scene-average spectrum, relative-reflectance spectra for the Kayenta, Chinle, White Rim, and Organ Rock Formations show absorption bands and/or "shoulders" near 0.55 μm that are attributable to crystalline ferric ions (Fe^{+3}) in these units. The relative-reflectance spectrum for the Moenkopi Formation is much brighter than average at short wavelengths and shows a small "shoulder" at 0.55 μm that may also be attributed to the crystalline ferrous ion. Calibrated spectra for these formations have similar features: the Kayenta, Chinle, White Rim, and Organ Rock Formations show relatively well defined absorption bands at ~0.55 μm, and the Moenkopi Formation shows no significant band at 0.55 μm. Relative-reflectance spectra for the Kayenta and Chinle Formations

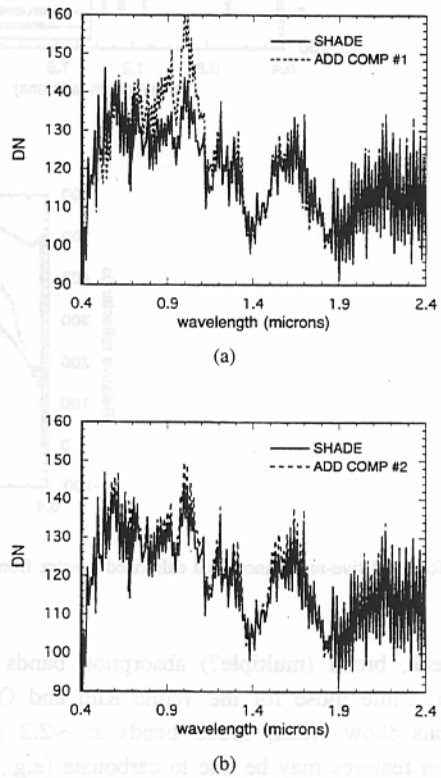

Fig. 12. AVIRIS spectra from Upheaval Dome, UT. Comparison of a "shade" spectrum and two calculated additive-component spectra for separate image sites [(a) and (b)]. Note that in (b), the shade spectrum and the additive-component #2 spectrum are very similar.

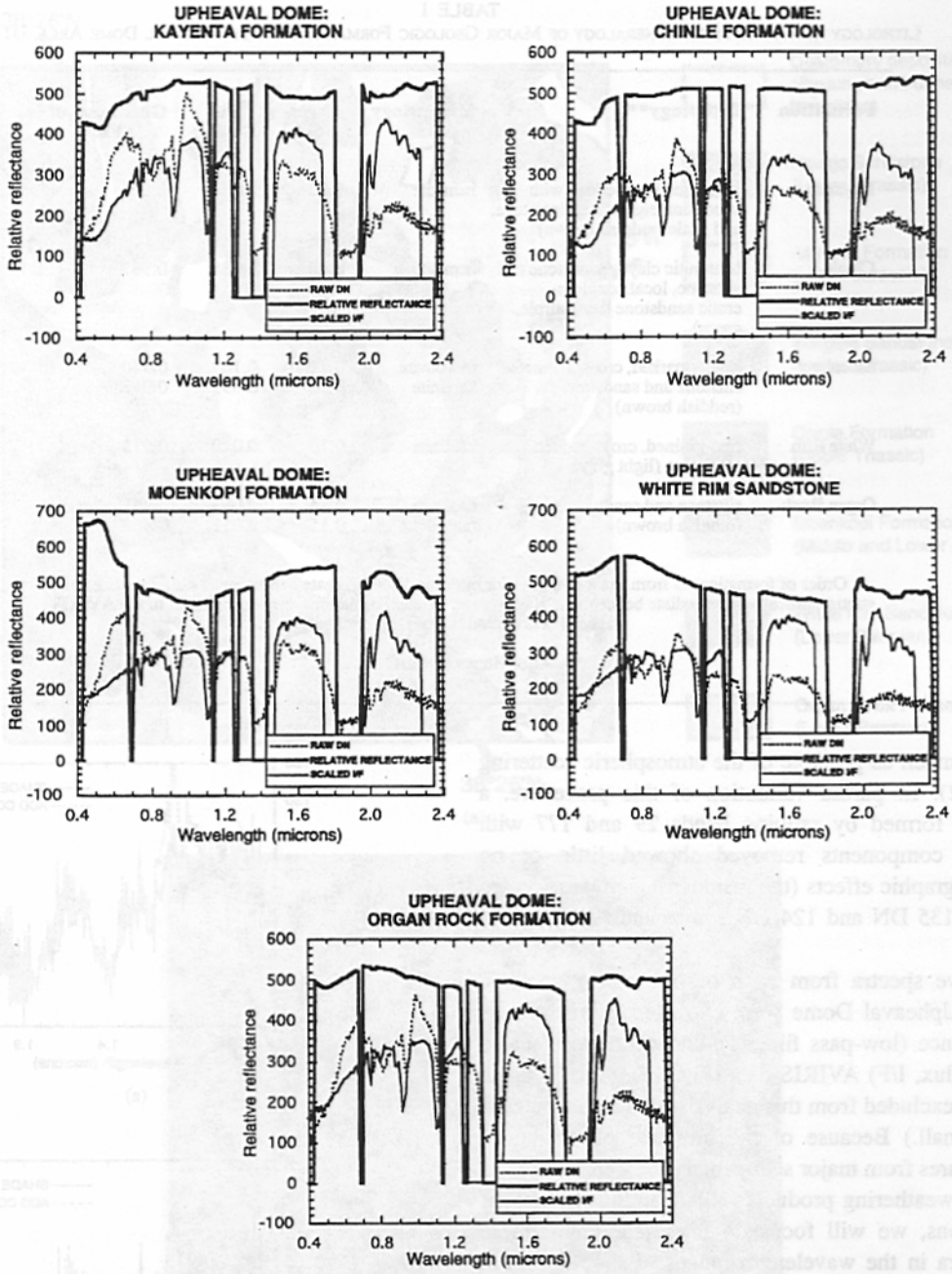

Fig. 13. Raw, relative-reflectance, and calibrated spectra from five major geologic formations of the Upheaval Dome, UT.

show weak, broad (multiple?) absorption bands at ~2.25-2.28 μm, while those for the White Rim and Organ Rock Formations show weak, broad bands at ~2.2 μm. These absorption features may be due to carbonate (e.g., calcite) or clay (e.g., kaolinite) minerals in these formations, respectively. The relative-reflectance spectrum for the Moenkopi Formation shows a pronounced absorption band at 2.2 μm that may be indicative of the presence of clay minerals (e.g., kaolinite). At longer wavelengths, calibrated spectra show more complex, stronger absorption features at 2.2 μm, but in all cases they correspond closely to the relative-reflectance spectra (Fig. 13). Note that 2.3-μm data are not available for comparison in the calibrated data.

Using the spectral library of the U.S. Geological Survey in Denver and the "Multiple Spectral Feature Mapping Algorithm" (MSFMA; [33], [34]), Clark *et al.* [19] have detected several major minerals and their relative proportions in many of the formations of Upheaval Dome (all results described in this paragraph are theirs). The MSFMA maps different geologic units through detection of individual minerals and determination of their proportions by comparison with a reference spectrum for each unit. In the Kayenta

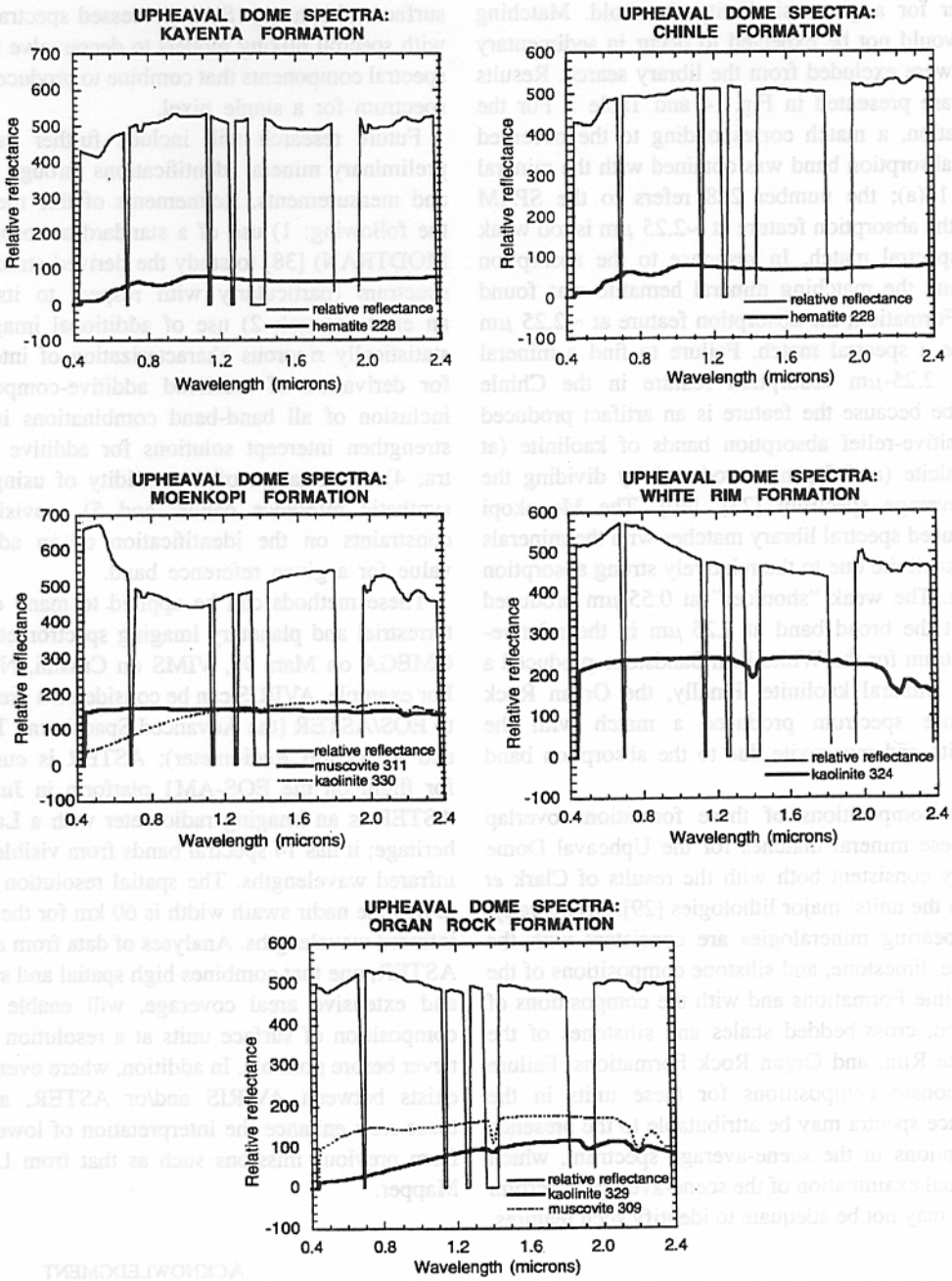

Fig. 14. Relative reflectance and "matching" laboratory spectra (from the SPAM spectral library) from five major geologic formations of the Upheaval Dome area, UT.

Formation, medium-intensity absorption bands for hematite (Fe_2O_3, with an Fe^{+3} absorption "shoulder" at 0.55 μm and an Fe^{+3} band at 0.9 μm) and calcite ($CaCO_3$, with weak CO_3 bands at 2.35 μm; [35]) were detected; trace-intensity bands were detected for kaolinite ($Al_2Si_2O_5(OH)_4$, with hydroxyl bands at 2.2 μm). Strong absorption bands for muscovite ($KAl_3Si_3O_{10}(OH)_3$, with hydroxyl bands at 2.2 μm) and hematite were detected in the Chinle Formation, as were weak absorptions for kaolinite and calcite. Medium-intensity hematite and muscovite, weak kaolinite, and trace calcite absorption bands were detected in the Moenkopi Formation. Mineralogical data were not cited by Clark *et al.* [19] for other Upheaval Dome units. Differences in absorption-band strengths are attributed to abundance changes.

To identify possible mineral components, a spectrum-matching technique was applied to each of the representative spectra from major geologic formations at Upheaval Dome and used to search through the SPAM spectral library [36] in the separate wavelength ranges of 0.45–0.65 and 2.0–2.3 μm. A spectral band-depth analysis algorithm [24], [37] was used to compute the band depth of an observed absorption feature relative to its continuum and to calculate a goodness-

of-fit parameter for a given similarity threshold. Matching minerals that would not be expected to occur in sedimentary geologic units were excluded from the library search. Results of this search are presented in Fig. 14 and Table I. For the Kayenta Formation, a match corresponding to the observed 0.55-μm Fe^{+2} absorption band was obtained with the mineral hematite (Fig. 14(a); the number 228 refers to the SPAM library index); the absorption feature at ~2.25 μm is too weak to produce a spectral match. In response to the absorption band at 0.55 μm, the matching mineral hematite was found for the Chinle Formation; the absorption feature at ~2.25 μm did not produce a spectral match. Failure to find a mineral match for this 2.25-μm absorption feature in the Chinle spectrum may be because the feature is an artifact produced by inverse, positive-relief absorption bands of kaolinite (at 2.2 μm) and calcite (at 2.3 μm) introduced by dividing the scene by an average spectrum [23], [40]. The Moenkopi Formation produced spectral library matches with the minerals muscovite and kaolinite due to the relatively strong absorption band at 2.2 μm. The weak "shoulder" at 0.55 μm produced no matches, but the broad band at 2.25 μm in the relative-reflectance spectrum for the White Rim Sandstone produced a match with the mineral kaolinite. Finally, the Organ Rock relative-reflectance spectrum produced a match with the minerals kaolinite and muscovite due to the absorption band at 2.2 μm.

Although the compositions of these formations overlap considerably, these mineral matches for the Upheaval Dome units are broadly consistent both with the results of Clark *et al.* [19] and with the units' major lithologies [29]. Specifically, iron- and clay-bearing mineralogies are consistent with the marine sandstone, limestone, and siltstone compositions of the Kayenta and Chinle Formations and with the compositions of the ripple-marked, cross-bedded shales and siltstones of the Moenkopi, White Rim, and Organ Rock Formations. Failure to identify carbonate compositions for these units in the relative-reflectance spectra may be attributable to the presence of calcite absorptions in the scene-average spectrum, which suggests that visual examination of the scene-average spectrum alone (Fig. 9(b)) may not be adequate to identify such features.

VI. Summary and Conclusion

Although these results are preliminary, they demonstrate our success in extracting reasonable mineral signatures from complex AVIRIS data. We first described a technique for derivation of an additive-component spectrum. Use of this technique not only allows decoupling of atmospheric scattering from surface reflectance, it also provides an independent check on the behavior of the instrument through analyses of instrument dark-current behavior (i.e., if the atmospheric scattering component of the total additive spectrum can be decomposed into instrument dark-current and Rayleigh and Mie scattering components, then the instrument dark current can be studied). Treatment of the multiplicative components of the measured AVIRIS spectra has allowed extraction of surface-reflectance data that can be interpreted in terms of surface mineralogy. Such processed spectra can then be used with spectral mixing models to deconvolve them into possible spectral components that combine to produce a given measured spectrum for a single pixel.

Future research will include further validation of these preliminary mineral identifications through field observations and measurements. Refinements of this method will include the following: 1) use of a standard atmospheric model (e.g., MODTRAN) [38] to study the derived atmospheric scattering spectrum (particularly with respect to its variability over an entire scene); 2) use of additional image sites for more statistically rigorous characterization of intercept values and for derivation of localized additive-component spectra; 3) inclusion of all band-band combinations in matrix form to strengthen intercept solutions for additive component spectra; 4) examination of the validity of using multiple and/or synthetic reference bands; and 5) provision of additional constraints on the identification of an additive-component value for a given reference band.

These methods can be applied to many of the anticipated terrestrial and planetary imaging spectrometer data sets (e.g., OMEGA on Mars 96, VIMS on Cassini, NIMS on Galileo). For example, AVIRIS can be considered a precursor instrument to EOS/ASTER (the Advanced Spaceborne Thermal Emission and Reflection Radiometer); ASTER is currently scheduled for flight on the EOS-AM1 platform in June of 1998 [39]. ASTER is an imaging radiometer with a Landsat and SPOT heritage; it has 14 spectral bands from visible through thermal infrared wavelengths. The spatial resolution of ASTER is 15 m and the nadir swath width is 60 km for the visible and near-infrared wavelengths. Analyses of data from an instrument like ASTER, one that combines high spatial and spectral resolution and extensive areal coverage, will enable mapping of the composition of surface units at a resolution and to an extent never before possible. In addition, where overlapping coverage exists between AVIRIS and/or ASTER, analyses such as these may enhance the interpretation of lower resolution data from previous missions such as that from Landsat Thematic Mapper.

Acknowledgment

The authors would like to thank R. Clark, P. Davis, and three anonymous reviewers for providing thoughtful and very helpful technical reviews.

References

[1] P. Switzer, W. S. Kowalik, and R. J. P. Lyon, "Estimation of atmospheric path-radiance by the covariance matrix method," *Photogrammetric Eng. Remote Sensing*, vol. 47, no. 10, pp. 1469–1476, 1981.

[2] W. S. Kowalik, R. J. P. Lyon, and P. Switzer, "The effects of additive radiance terms on ratios of Landsat data," *Photogrammetric Eng. Remote Sensing*, vol. 49, no. 5, pp. 659–669, 1983.

[3] R. E. Crippen, "The regression intersection method of adjusting image data for band ratioing," *Int. J. Remote Sensing*, vol. 8, no. 2, pp. 137–155, 1987.

[4] P. S. Chavez, "An improved dark-object subtraction technique for atmospheric scattering correction of multispectral data," *Remote Sensing Environ.*, vol. 24, pp. 459–479, 1988.

[5] ——, "Radiometric calibration of Landsat thematic mapper multispectral images," *Photogrammetric Eng. Remote Sensing*, vol. 55, pp. 1285–1294, 1989.

[6] R. O. Green, "Radiative transfer based retrieval of reflectance from calibrated radiance imagery measured by an imaging spectrometer for lithological mapping of the Clark Mountains," in *Imaging Spectroscopy of the Terrestrial Environment*. Bellingham, WA: SPIE, vol. 1298, pp. 213–221, 1990.

[7] F. A. Kruse, A. B. Lefkoff, and J. B. Dietz, "Expert system-based mineral mapping in Northern Death Valley," California/Nevada, using the airborne visible/infrared imaging spectrometer (AVIRIS), *Remote Sensing Environ.*, vol. 44, pp. 309–336, 1993.

[8] G. Vane, Ed., *Airborne Visible/Infrared Imaging Spectrometer (AVIRIS)*. Pasadena, CA: JPL, 1987 (JPL Publication 87-38).

[9] G. Vane, R. O. Green, T. G. Chrien, H. T. Enmark, E. G. Hansen, and W. M. Porter, "The airborne visible/infrared imaging spectrometer (AVIRIS)," *Remote Sensing Environ.*, vol. 44, pp. 127–143, 1993.

[10] T. G. Chrien, R. O. Green, and M. L. Eastwood, "Accuracy of the spectral and radiometric laboratory calibration of the airborne visible/infrared imaging spectrometer (AVIRIS)," in *Imaging Spectroscopy of the Terrestrial Environment*. Bellingham, WA: SPIE, vol. 1298, pp. 37–49, 1990.

[11] R. O. Green, S. A. Larson, and H. I. Novack, "Calibration of AVIRIS digitized data," in *Proc. 3rd Airborne Visible/Infrared Imaging Spectrometer (AVIRIS) Workshop*, 1991, pp. 109–118 (JPL Publication91-28).

[12] P. N. Slater, F. J. Doyle, N. L. Fritz, and R. Welch, "Photographic systems for remote sensing," in *Manual of Remote Sensing*, 2nd ed. Falls Church, VA: Amer. Soc. Photogrammetrty, 1983, vol. 1, ch. 6, pp. 231–291.

[13] J. P. Peixoto and A. H. Oort, *Physics of Climate*. New York: Amer. Inst. Phys., 1992, p. 456.

[14] B. Hapke, *Theory of Reflectance and Emittance Spectroscopy*. New York: Cambridge Univ. Press, 1993, p. 455.

[15] E. M. Shoemaker and K. E. Herkenhoff, "Upheaval dome impact structure," *Lunar and Planetary Science XV*. Houston, TX: Lunar Planetary Inst., 1984, pp. 778–779.

[16] E. T. McKnight, "Geology of area between Green and Colorado rivers," Grand and San Juan counties, Utah, *U.S. Geological Survey Bull. 908*, p. 147, 1940.

[17] W. H. Press, B. P. Flannery, S. A. Teukolsky, and W. T. Vetterling, *Numerical Recipes*. Cambridge, England: Cambridge Univ. Press, 1986, p. 818.

[18] F. A. Kruse, "Use of airborne imaging spectrometer data to map minerals associated with hydrothermally altered rocks in the Northern Grapevine Mountains," Nevada and California, *Remote Sensing Environ.*, vol. 24, pp. 31–51, 1988.

[19] R. N. Clark, G. A. Swayze, and A. Gallagher, "Mapping the mineralogy and lithology of Canyonlands, Utah, with imaging spectrometer data and the multiple spectral feature mapping algorithm," in *Summaries of the 3rd Annu. Airborne Geosciences Workshop*, 1992, vol. 1, pp. 11–13 (JPL Publication 92-14).

[20] H. R Joesting, J. E. Case, and D. Plouff, "Regional geophysical investigations of the Moab-Needles area," Utah, *U.S. Geological Survey Prof. Paper 516-C*, vol. C1-C21, 1967.

[21] W. H. Bucher, "Cryptovolcanic structures in the United States," in *Int. Geological Congr., 16th, Washington, 1933, Reports*, 1936, vol. 2, pp. 1055–1084.

[22] J. D. Boon and C. C. Albritton, "Meteorite craters and their possible relationship to 'cryptovolcanic structures,'" *Field Lab.*, vol. 5, pp. 1–9, 1936.

[23] R. N. Clark and T. V. V. King, "Causes of spurious features in spectral reflectance data," in *Proc. 3rd Airborne Imaging Spectrometer Data Analysis Workshop of Geophysical Research*, 1987, pp. 132–137 (JPL Publication 87-30).

[24] R. N. Clark and T. L. Roush, "Reflectance spectroscopy: Quantitative analysis techniques for remote sensing applications," *J. Geophys. Res.*, vol. 89, no. B7, pp. 6329–6340, 1984.

[25] R. V. Morris, S. C. Neely, and W. W. Mendell, "Application of Kubelka-Munk theory of diffuse reflectance to geologic problems: The role of scattering," *Geophys. Res. Lett.*, vol. 9, pp. 113–116, 1982.

[26] T. B. McCord, R. N. Clark, B. R. Hawke, L. A. McFadden, P. D. Owensby, C. M. Pieters, and J. B. Adams, "Moon: Near-infrared reflectance, a first good look," *J. Geophys. Res.*, vol. 86, pp. 10 883–10 892, 1981.

[27] R. B. Singer, "Spectroscopic observations of Mars," *Adv. Space Res.*, vol. 5, pp. 59–68, 1985.

[28] E. M. Shoemaker, "Structural features of the central Colorado Plateau and their relation to uranium deposits," *U.S. Geological Survey Prof. Paper 300*, pp. 155–170, 1956.

[29] P. W. Huntoon, G. H. Billingsley, and W. J. Breed, *Geologic Map of Canyonlands National Park and Vicinity*, The Canyonlands Natural History Association, UT, 1982.

[30] G. R. Hunt and J. W. Salisbury, "Visible and near-infrared spectra of minerals and rocks: I silicate minerals," *Modern Geology*, vol. 1, pp. 283–300, 1970.

[31] ——, "Visible and near-infrared spectra of minerals and rocks: VI additional silicates," *Modern Geol.*, vol. 4, pp. 85–106, 1973.

[32] G. R. Hunt, J. W. Salisbury, and C. J. Lenhoff, "Visible and near-infrared spectra of minerals and rocks: III oxides and hydroxides," *Modern Geol.*, vol. 2, pp. 195–205, 1971.

[33] R. N. Clark, A. J. Gallagher, and G. A. Swayze, "Material absorption band depth mapping of imaging spectrometer data using a complete band shape least-squares fit with library reference spectra," in *Proc. 2nd AVIRIS Workshop*, 1990a, pp. 176–186 (JPL Publication 90-54).

[34] R. N. Clark, G. A. Swayze, A. Gallagher, N. Gorelick and F. Kruse, "Mapping with imaging spectrometer data using the complete band shape least-squares algorithm simultaneously fit to multiple spectral features from multiple materials," in *Proc. 3rd AVIRIS Workshop*, 1991, vol. 2–3.

[35] S. J. Gaffey, "Reflectance spectroscopy of carbonate minerals and rocks in the visible and near infrared: Potential as a tool for geologic mapping and exploration," in *Proc. 3rd Thematic Conference on Geologic Remote Sensing*, 1984, pp. 865–874.

[36] C. Grove, S. Hook, and E. Paylor, "Laboratory reflectance spectra of 160 minerals (0.4 to 2.5 micrometers)," Jet Propulsion Lab., Pasadena, CA, JPL Publication 92-2, p. 208, 1992.

[37] R. N. Clark, T. V. V. King, M. Klejwa, and G. A. Swayze, "High spectral resolution reflectance spectroscopy of minerals," *J. Geophys. Res.*, vol. 95, no. B8, pp. 12 653–12 680, 1990b.

[38] A. Berk, L. S. Bernstein, and D. C. Roberson, *MODTRAN: A Moderate Resolution Model For LOWTRAN-7*. Hanscom Air Force Base, MA: U.S. Air Force Geophys. Lab., 1989.

[39] G. Asrar and J. Dozier, *Science Strategy for the Earth Observing System*. Woodbury, NY: Amer. Inst. Phys. Press, 1994.

[40] R. Clark, personal communication, 1993.

Lisa R. Gaddis received the A.B. degree in geology from Vassar College, Poughkeepsie, NY, in 1979, the M.Sc. degree in geological sciences from Brown University, Providence, RI, in 1981, and the Ph.D. degree in geology and geophysics from the University of Hawaii in 1987. Her dissertation involved radar and spectral reflectance studies of volcanic terrains on the Earth and the Moon.

Following a postdoctoral position at Arizona State University (where she was involved in field and remote sensing data acquisition projects that were SIR-C precursors), she joined the Astrogeology Branch of the U.S. Geological Survey in Flagstaff in 1990. As a Research Geologist, her current projects include analyses of AIRSAR data for characterization and modeling of scattering properties of geologic units; use of Magellan radar data and debris-flow modeling for geologic studies of crater outflows on Venus; studies of AVIRIS hyperspectral data to remove instrument and atmospheric effects for extracting mineral signatures in arid environments; and calibration and use of SSI data from NASA Galileo mission to the Moon for mapping the composition of lunar deposits.

Laurence A. Soderblom received the Ph.D. degree in planetary science and geophysics from the California Institute of Technology, Pasadena, in 1970.

He has worked as a Research Geophysicist in the Astrogeology Branch of the U.S. Geological Survey since 1970. His work activities include extensive involvement with planning and implementation of NASA missions (e.g., instrument design, mission planning, data acquisition and analysis for Voyager, Magellan, Galileo NIMS, Cassini, Mars Pathfinder, etc.), scientific research on volcanism on Io, volatiles of the Martian South Polar region, the Uranian satellites, and Triton, a moon of Neptune, and development and distribution of the USGS ISIS image processing software.

Hugh H. Kieffer received the Ph.D. degree in planetary science from the California Institute of Technology, Pasadena, in 1968.

He has been a Research Geophysicist in the Astrogeology Branch of the U.S. Geological Survey since 1978. His work activities have focused on instrument design and characterization for numerous terrestrial and planetary missions, including Mariner, Viking, Galileo, Mars Global Surveyor, Landsat, HIRIS, ASTER, AVIRIS, and HYDICE. His scientific research interests have included topics as diverse as measurement of thermal infrared radiation at Mount St. Helens and on Mars, characterization of radiometric performance of Landsat Thematic Mapper, and development of a lunar observatory for calibration of multispectral data.

Kris J. Becker received the B.S. degree in mathematics and computer science from Northern Arizona University, Flagstaff, in 1986.

He has worked as a Computer Scientist in the Astrogeology Branch of the U.S. Geological Survey since 1985. Most recently, he has focused his work efforts on engineering research and development of the Integrated Software for Imaging Spectrometers (ISIS) software system in use at the USGS/Flagstaff. He has also been the lead software engineer and team leader for the design and implementation of a real-time data collection system for an Earth- based lunar robotic telescope.

James Torson received the B.S. degree in engineering and computer science from Case Western Reserve University, Cleveland, OH, in 1969.

He has worked as a Computer Software Engineer in the Astrogeology Branch of the U.S. Geological Survey since 1985. His primary focus has been on the design and implementation of the ISIS software system, particularly interactive 3-D cube data display, in support of planetary cartography and science research at the USGS/Flagstaff.

Kevin Mullins received the B.S. degree in geology and remote sensing at Northern Arizona University, Flagstaff, in 1986 and the M.A.T. degree in 1995.

He has worked as a Geologist in the Astrogeology Branch of the U.S. Geological Survey since 1979. His work includes assessment of instrument response, correlation of instrument and laboratory spectra with field sample spectra, identification and mapping of geologic units using remote sensing data, and radiometric, photogrammetric, and cartographic digital processing of data from numerous NASA missions.